New generation photon-counting cameras: algol and CPNG

Alain Blazit,[1,*] Xavier Rondeau,[2,3,4,5] Éric Thiébaut,[2,3,4,5] Lyu Abe,[1] Jean-Claude Bernengo,[6] Jean-Louis Chevassut,[1] Jean-Michel Clausse,[1] Jean-Pierre Dubois,[2,3,4,5] Renaud Foy,[2,3,4,5,7] Denis Mourard,[1] Fabien Patru,[1] Alain Spang,[1] Isabelle Tallon-Bosc,[2,3,4,5] Michel Tallon,[2,3,4,5] Yves Tourneur,[6] and Farrokh Vakili[1]

[1]UMR 6525 H. Fizeau, Université de Nice-Sophia Antipolis, Centre National de la Recherche Scientifique, Observatoire de la Côte d'Azur, Campus Valrose, F-06108 Nice Cedex, France

[2]Université de Lyon, Lyon, F-69000, France

[3]Université Lyon 1, Villeurbanne, F-69622, France

[4]Centre de Recherche Astronomique de Lyon, Observatoire de Lyon, 9 avenue Charles André, Saint-Genis Laval cedex, F-69561, France

[5]CNRS/UMR-5574, Ecole Normale Supérieure de Lyon, Lyon, France

[6]CCQ-UCBL, Université de Lyon, Lyon, F-69000, France; Université Lyon 1, Villeurbanne, F-69622, France

[7]Observatoire de Haute Provence—CNRS, 04870 Saint-Michel l'Observatoire, France

*Corresponding author: alain.blazit@obs-azur.fr

Algol and Comptage de Photons Nouvelle Génération (CPNG) are new generation photon counting cameras developed for high angular resolution in the visible by means of optical aperture synthesis and speckle interferometry and for photon noise limited fast imaging of biological targets. They are intensified CCDs. They have been built to benefit from improvements in photonic commercial components, sensitivity, and personal computer workstations processing power. We present how we achieve optimal performances (sensitivity and spatiotemporal resolution) by the combination of proper optical and electronics design, and real-time elaborated data processing. The number of pixels is 532×516 and 1024^2 read at a frame rate of 262 and $100\,\mathrm{Hz}$ for CPNG and Algol, respectively. The dark current is very low: $5.5 \times 10^{-4}\,e^-$ .pixel^{-1}. s^{-1}. The saturation flux is ≈ 7 photon events /pixel/s. Quantum efficiencies reach up to 36% and 26% in the visible with the GaAsP photocathodes and in the red with the GaAs ones, respectively, thanks to the sensitivity of the photocathodes and to the photon centroiding algorithm; they are likely the highest values reported for intensified CCDs. © 2008 Optical Society of America

OCIS codes: 040.0040, 030.5260, 100.6640.

1. Introduction: Needs and Specifications

Photon-counting detectors aim at providing images characterized both by particularly low readout and thermal noises and by fast frame rates. They are dedicated to the imaging of low light level sources.

In this paper when we refer to a photon-counting detector, we mean a device able to detect the position and arrival time of any single photon event in the image. This is different from a CCD, which counts the only integrated number of photons stored per pixel.

We report the specifications and performances of the new generation Algol and CPNG cameras, which we have developed. They are intensified CCDs. They

are both dedicated to high angular resolution imaging in astrophysics and to fast imaging at a low light level in cytobiology.

Since 1974 we have used photon-counting cameras to observe astrophysical sources at high angular resolution, mostly with Michelson interferometry and speckle interferometry. For this purpose, we had CP40 built [1,2], a previous generation of intensified CCD (ICCD) with 1536×1152 pixels read at 50 Hz per frame. Its quantum efficiency had decreased from $\approx 8 - 10\%$ down to $\lesssim 4\%$ because of aging. The resulting limiting magnitude at the GI2T-REGAIN interferometer [3] was $\lesssim 6$. With the speckle interferometer differential (SPID) speckle interferometer [4], it ranged from $\lesssim 10.5$ to ≈ 16.5 for spectral resolutions of 3000 and 300, respectively. This sensitivity is markedly too low by at least 2 astronomical magnitudes for many high priority science cases of high angular resolution observations, e.g., as extragalactic sources and pre-main-sequence stars.

Interferometric observations in the visible range need detectors faster than 50 Hz to get the optimal signal-to-noise ratio (SNR) on the interference contrasts under the most common turbulence conditions. Typically a 250 Hz frame rate is required. The spatial resolution must be at least 800×800 pixels for the visible spectrograph and polarimeter (VEGA) [5,6] interferometer to correctly sample the interference fringes and to have the whole image extension in the camera field. For SPID $\sim 1000 \times 1000$ pixels is required for its four simultaneous image channels. This can be achieved by means of super resolution processing techniques. To observe faint sources [7], we need a noise level lower than 2500 shots/s. We also need better operability (low weight, automatized cooling).

In life sciences, photon-counting imaging is now a routine technique in many fields, such as experimental cancer research. Most studies make use of the large number of insects, bacteria, and marine animals expressing luminescent proteins, which are absent in mammalians. The injection of luminescent cells into an animal [8,9], or the expression of luminescent proteins in a cell [10], provides a signal detectable with a high specificity. Specific photoproteins can probe calcium ions (aequorin), nicotinamide adenine dinucleotide (bacterial luciferase), superoxide free radicals (lucigenin), or adenosine triphosphate (ATP) (firefly luciferase). Photon-counting cameras are routinely used to monitor luminescent tumors in small animals [11]. In our university, we recently developed a photon-counting setup after the pioneering study of Maechler et al. [12]. Cells transfected to express the firefly luciferase emit photons proportionally to the available ATP concentration. The light is collected through a high numerical aperture microscope objective and directed toward the cathode of a photomultiplier. In these experiments at the cellular level, the main information is carried by the temporal signal, while the cells are submitted to different experimental conditions [12].

The challenge consists in replacing the photomultiplier by a photon imaging device without losing the real-time monitoring signal of photon emission [13]. At high magnification, a microscope has a poor numerical aperture so that it does not require a high spatial resolution, but the time occurrence of photon emission may carry useful information. These requirements may not be fulfilled by a classical integrating camera.

Photon-counting cameras made in the industry are either too slow (TV speed) or with a relatively low quantum efficiency (using an S20 photocathode instead of a GaAs or GaAsP). For example, Gach et al. [14] built a sensitive camera, but not fast enough, only 80 img/s at maximum speed. Electron multiplier CCDs (EMCCD), also referred to as low light level CCDs (LLLCCD) rely on a new CCD technology [15,16], which appeared a few years ago. EMCCDs have an amplification register before the readout amplifier, which provides intensification of the charge packets by avalanches between electrodes of the register. The gain is sufficient for photon-counting operation for astrophysical applications [17,18] as well as for biological ones [19]. Gach et al. have already tested such a camera for astronomical applications [20]. We also made some experiments at Observatoire de Haute Provence (OHP) in collaboration with the Laboratoire d'Interférométrie Stellaire et Exoplanétaire (LISE) team, using Andor iXon cameras and at Lyon Observatory with a Roper Scientific "cascade" camera. Clock induced charges appear in the CCD array; they are amplified like the photoelectrons and produce noise. We have measured that the EMCCD architecture produces $0.5 e^-$ per pixel per frame; this is above our required specification by at least a factor of 100. Moreover, with EMCCDs, it is impossible to perform super resolution: detected photon events spread over only one pixel, which prevents better position determination. Finally, existing cameras based on this technique are not fast enough for our needs. Since current EMCCD technology does not match our requirements, we have designed and built Algol and CPNG ICCDs to match the requirements of both domains of biological and astronomical applications.

In the following, we describe the hardware design of the cameras, we explain the real-time data processing, and finally, we present the measured performances of our CPNG cameras.

2. Hardware Design

To enable faster buildup, flexible data processing, and easier upgrade and maintenance, we choose a modular hardware design (cf. Fig. 1) with standard components.

A. Photonic Components

In an ICCD, the effective quantum efficiency (QE) and the spectral response are determined by the characteristics of the first intensifier photocathode. Depending on the readout noise of the CCD,
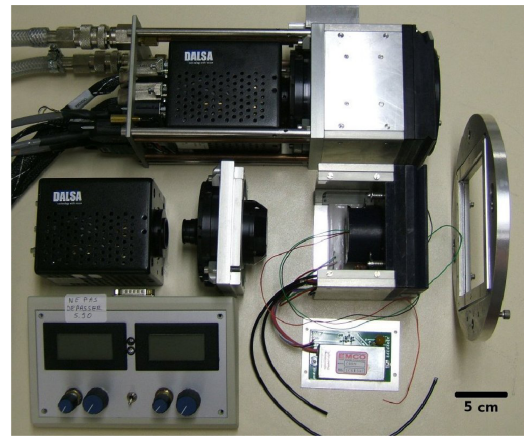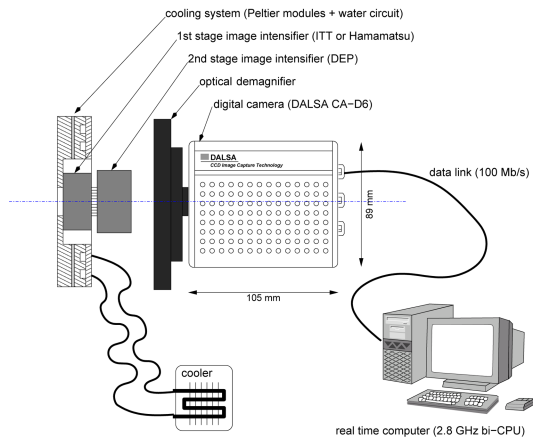
Fig. 1. (Color online) Left: Hardware design of a CPNG. Right: an assembled (top) and a dismantled (bottom) CPNG camera.

additional secondary intensifiers may be required to provide sufficient light amplification to overcome the CCD noise. Algol and CPNG are designed from commercial on-the-shelf components.

Our principal need is sensitivity, and we selected first stage image intensifiers from their photocathode. As a single photocathode cannot completely cover our spectral range, we decided to build cameras with two different first stage intensifiers:

• Hamamatsu V8070U-64 with GaAsP photocathode providing a QE between 40% and 50% in the blue-visible region, 425–650 nm, and a resolution of 51 line pairs per millimeter (lp/mm);
• ITT FS9910 with GaAs photocathode providing a QE between 30% and 40% in the red domain, 520–850 nm, and a resolution of 64 lp/mm.

The additional secondary intensifier, which provides us with an additional gain, is a Photonis XX1450VN with an internal power supply. It has 58 line pairs(lp)/mm, which does not reduce the achievable resolution. The useful diameter of the photocathodes of the selected light amplifiers is 18 mm.

To focus the intensified image on the CCD, we use a Rodenstock Heligaron coupling lens ($F/1.55$) with adjustable image magnification. For comparable light loss, lens coupling avoids image distortion and microdislocations by fiber optics coupling. Moreover, the adjustable image magnification is of particular interest for proper sampling of the events. This is required to achieve subpixel resolution as explained in Section 3.

The readout cameras are coupled to the lens by their C-mounts and can be exchanged with other cameras as needed. For our applications, we have chosen the following readout cameras (mainly based on their frame rate and number of pixels):

• for SPID and biological applications, the CPNG camera is equipped with a DALSA CA-D6; it is an 8 bit digital CCD camera with 532×516 pixels and a frame rate of 262 img/s;

• for VEGA [5,6], the Algol camera is equipped with a DALSA 1M150; it is an 8 bit digital complementary metal-oxide semiconductor (CMOS) camera with 1024×1024 pixels from which we use only 800×600 and a frame rate of 50 or 100 img/s.

B. Surroundings

To reduce the thermal current noise, the first semiconductor photocathode must be cooled (noisy events from the photocathode of the second intensifier undergo insufficient amplification so that thermal emission of the second intensifier can be neglected). In our cameras, the cooling is ensured by ten thermoelectric Peltier modules with cold water circulation for heat dissipation. The temperature is set to $-15\,°C$ for GaAsP photocathodes and $-35\,°C$ for GaAs ones (Subsection 4.A). It is measured and tuned with a $0.3\,°C$ accuracy thanks to a programmable temperature controller. The input window of the first intensifier can be flushed by dry air circulation to remove moisture and avoid frost formation. The gains of both intensifiers are manually or computer controlled.

C. Data Processing Components

Photon-counting data processing of the intensified images consists in the detection and localization of the photon events. With our fast frame rates, it is not possible to save all pixel values. However, only a small fraction of the pixels contains a significant signal. Real-time detection of the photon events is required to reduce the amount of data. Owing to the high pixel rate (up to 72×10^6 pixels/s for CPNG), such a processing is CPU demanding; nevertheless we have developed fast enough algorithms to perform this computation with a 3 GHz Intel Pentium 4 without dedicated programmable electronic devices [such as a digital signal processor (DSP) or field programmable gate array (FPGA)]. The computational tasks are:

• images acquisition, without any loss
• preprocessing of images: deinterleaving and background subtractions

- photon events detection and subpixel localization
- real-time photon events visualization to survey data acquisition and proper camera operation,
- storage of photon events positions and intensities in 3×3 or 5×5 pixel boxes for posterior processing.

3. Optimal Detection and Fine Centering of the Photon Events

The intensified events are seen by the CCD as more or less bright spots. The "energetic distribution" of local maxima in the raw ICCD images is shown in Fig. 2. The peak around 0 Digital Units (DU) in the histogram is mostly due to the readout noise of the CCD. The tail of the distribution at high DU values corresponds to the intensified events.

The events "spatial brightness distribution," due to the intensifier stages and the optical coupling, can be a key point regarding detection and superresolution (subpixel localization of events). On the one hand, if an event spreads over less than a CCD pixel, then its detection among the CCD background noise is easier, because the peak pixel intensity is maximized, but its position cannot be more precise than a pixel. On the other hand, if the event is larger than a CCD pixel, then its spatial spreading makes it possible to achieve subpixel resolution by means of centroiding techniques, but the detection efficiency is reduced by the flux dilution with respect to the CCD readout noise. Moreover, wider events yield a larger so-called "photon-counting hole" [2,21,22], which is a wider area, where only one photon can be detected, which limits the saturation flux of the detector. Since we wanted to achieve reliable subpixel resolution, whereas keeping good detection efficiency and a good saturation flux, we designed
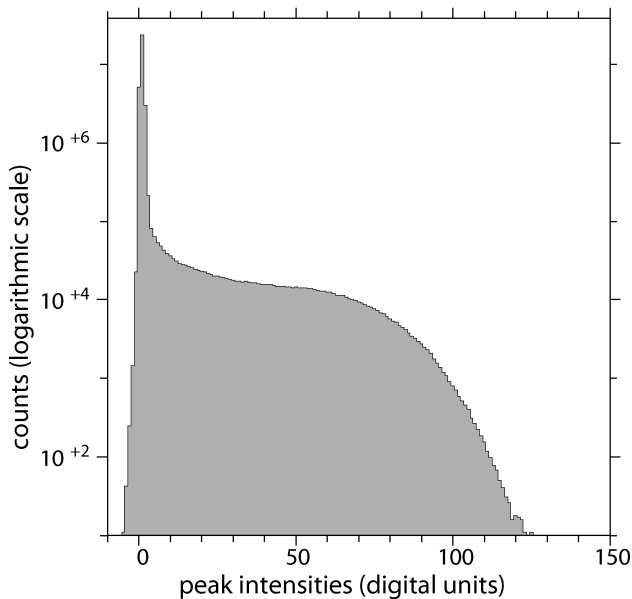

Fig. 2. Continues on facing page.

the hardware to have the proper tradeoff between these effects.

A. Photon-Event Shape

Figure 3 shows the measured average profile of the photon events. It has been obtained by averaging a few ten thouthands of recentered (at 1/100th pixel precision) events. The full width at half maximum (FWHM) depends on three factors: the spread of the photon burst at the output of the intensifiers, the focalization by the coupling lens, and the CCD pixel size. Assuming that the 2D brightness distribution $s(\Delta x, \Delta y)$ is separable (which is well verified in practice as can be observed from Fig. 3), it can be written as $s(\Delta \mathbf{x}) = s(\Delta x)s(\Delta y)$, where $\Delta \mathbf{x} = (\Delta x, \Delta y)$ are the coordinates with respect to the peak of the photon event. Further assuming that it is approximately Gaussian (which can also be observed from Fig. 3) with FWHM ω and that the response of the CCD is uniform within each pixel, then the 1D distribution writes

$$
\begin{aligned}
s(\Delta x) &= \int_{\Delta x - a/2}^{\Delta x + a/2} \exp\left(-\log 16 \frac{u^2}{\omega^2} \right) \mathrm{d}u \\
&= \frac{1}{2} \left[\mathrm{erfc}\left(\frac{\sqrt{\log 16}}{\omega} \left(\Delta x - \frac{a}{2} \right) \right) \right. \\
&\quad \left. - \mathrm{erfc}\left(\frac{\sqrt{\log 16}}{\omega} \left(\Delta x + \frac{a}{2} \right) \right) \right],
\end{aligned}
\tag{1}
$$

where a is the size of a pixel and $\mathrm{erfc}(z) = 1 - (2/\sqrt{\pi}) \int_0^z e^{-t^2} \mathrm{d}t$ is the complementary error function.

Using Eq. (1) and by numerical simulations, we found that a good tradeoff to preserve the efficiency of the detection, whereas achieving subpixel resolution and keeping a small photon-counting hole, is to tune the events FWHM in between 1.5 and 2 CCD pixels. Such events roughly spread over 3×3 CCD pixels. With our hardware settings, the actual shape of the real photon events matches this requirement with FWHM $\simeq 1.6$ pixels as shown by Fig. 3. After having tuned the focalization of the events with the optical coupling, we have measured that the shape of the events is almost invariant across the whole field of view.

In the following, we will show that an estimate of the photon-event shape is required to maximize the sensitivity of the detection and the accuracy of the event localization. Although we can use the real shape of the events as measured from real data, or the Gaussian approximation, we have seen that in practice, the cubic B-spline basis function b yields a suitable approximation with a finite size support as shown by Fig. 3

$$
s(\Delta x) \simeq b(\Delta x / w)
\tag{2}
$$

$$
\text{with} \quad b(u) = \begin{cases} 2/3 + (u/2 - 1)u^2 & \text{for } |u| \leq 1 \\ 1/6(2 - u)^3 & \text{for } 1 \leq |u| \leq 2 \\ 0 & \text{for } |u| \geq 2 \end{cases}
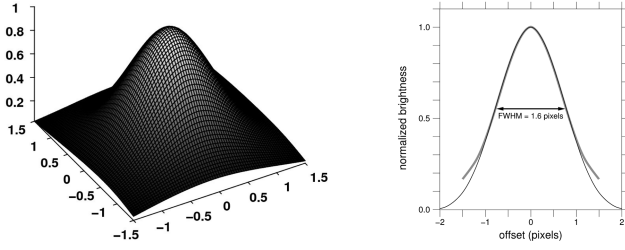$$

Fig. 3. Photon event shape. Left: measured mean 2D spatial brightness distribution of photon events on the readout CCD of CPNG. Right: mean 1D profile of real events (thick gray curve) and B-spline function (thin black curve).

where $w = \text{FWHM}_s/\text{FWHM}_b$ is the ratio of the FWHM of the event shape over that of the cubic B-spline, which is

$$\text{FWHM}_b = \frac{4}{3} + \frac{8}{3}\cos\left[\frac{\pi}{3} + \frac{1}{3}\tan^{-1}(3\sqrt{7})\right] \simeq 1.445. \quad (3)$$

B. Maximum Likelihood Detection

The first correction applied to the raw CCD images is background subtraction. The background level is quite large on the CCD or CMOS cameras in high sensitivity mode, but it remains stable. So we have measured it by averaging a few hundreds of images without intensifiers gain. On the DALSA CA-D6, there is a variable residual background after subtraction of the mean background. It is almost constant along a column. Since under low photon flux most of the CCD is dark, this columnwise residual background can be easily estimated and fixed. To that end, we subtract to every column (of every image) the level of the peak in the histogram of pixel values along that column. We use the mean event shape approximed in Eq. (2) to form the convolution kernel.

Owing to the shift-invariant point spread function of our ICCD, it is possible to model the corrected images $d(\mathbf{x})$ as

$$d(\mathbf{x}) = m(\mathbf{x}) + e(\mathbf{x}), \quad (4)$$

where $\mathbf{x} = (x, y)$ is the position on the CCD, $e(\mathbf{x})$ accounts for noise and modelization errors, and $m(\mathbf{x})$ is the "noiseless" model, which writes

$$m(\mathbf{x}) = \sum_k \alpha_k s(\mathbf{x} - \mathbf{x}_k), \quad (5)$$

where $\mathbf{x}_k$ is the central position of the kth event of the image and α_k is its brightness. Approximating the noise and modelization errors by white noise of variance $\text{var}[e(\mathbf{x})] = \sigma_{\text{CCD}}^2$, the best model parameters (i.e., brightness and position of the events), in the maximum likelihood sense, would be obtained by minimizing

$$\chi^2 = \frac{1}{\sigma_{\text{CCD}}^2}\sum_{\mathbf{x}}[d(\mathbf{x}) - m(\mathbf{x})]^2, \quad (6)$$

with respect to the α_ks and the $\mathbf{x}_k$s. A global fit of the image is however too CPU demanding and would not be applicable in real time. Nevertheless, at low photon counts, the events should be well separated in the observed image. If this is not the case, the overlapping of events would prevent their individual detection, according to the definition of the saturation flux for such a detector (see Subsection 5.A). Thus instead of minimizing the criterion given by Eq. (6) over the whole image, it is sufficient to apply the maximum likelihood principle "locally" around each event. For the kth event of the image, this means that one has to minimize

$$\chi_{\text{local}}^2(\mathbf{x}_k, \alpha_k) = \frac{1}{\sigma_{\text{CCD}}^2}\sum_{\mathbf{x}\in\mathcal{S}_k}[d(\mathbf{x}) - \alpha_k s(\mathbf{x} - \mathbf{x}_k)]^2, \quad (7)$$

where $\mathcal{S}_k$ is the event spatial support. In our case, $\mathcal{S}_k$ is the 3×3 or 5×5 pixel box centered at the event peak value. Since the response of our ICCD is shift invariant, we have

$$\mathbf{x}\in\mathcal{S}_k \Leftrightarrow \mathbf{x} - \mathbf{x}_k \in \mathcal{S},$$

where $\mathcal{S}$ is the support of the shape function s and χ_{local}^2 becomes

$$\chi_{\text{local}}^2(\mathbf{x}_k, \alpha_k) = \frac{1}{\sigma_{\text{CCD}}^2}\sum_{\Delta\mathbf{x}\in\mathcal{S}}[d(\mathbf{x}_k + \Delta\mathbf{x}) - \alpha_k s(\Delta\mathbf{x})]^2. \quad (8)$$

Partial minimization of the criterion in Eq. (8) with respect to α_k only yields the most likely kth event's brightness given its position

$$\alpha_k^+(\mathbf{x}_k) = \frac{\sum_{\Delta\mathbf{x}\in\mathcal{S}} d(\mathbf{x}_k + \Delta\mathbf{x})s(\Delta\mathbf{x})}{\sum_{\Delta\mathbf{x}\in\mathcal{S}} s(\Delta\mathbf{x})^2}. \quad (9)$$

Since $\sum_{\Delta\mathbf{x}\in\mathcal{S}} s(\Delta\mathbf{x})^2$ is constant, the events selected by maximum likelihood are local maxima of the function

$$d_s(\mathbf{x}) = \sum_{\Delta\mathbf{x}\in\mathcal{S}} d(\mathbf{x} + \Delta\mathbf{x})s(\Delta\mathbf{x}), \quad (10)$$

which is the discrete correlation of the detected image by the expected shape of the events. Owing to the small size of $\mathcal{S}$, this correlation can be computed in real time. Then the local maxima in $d_s(\mathbf{x})$ yield the positions of the events with a pixel precision.

According to our model, the expected value of the peak intensity of the kth event is $\langle d(\mathbf{x}_k)\rangle = \alpha_k s(\mathbf{0})$. Therefore, if local maxima are searched for in the raw image $d(\mathbf{x})$, then the detection SNR is

$$\text{SNR}_d = \frac{\langle d(\mathbf{x}_k)\rangle}{\sqrt{\text{var}[d(\mathbf{x}_k)]}} = \frac{\alpha_k}{\sigma_{\text{CCD}}}s(\mathbf{0}). \quad (11)$$

Under our Gaussian white noise approximation, the variance of the CCD intensity's values in the filtered image $d_s(\mathbf{x})$ is

$$\text{var}[d_s(\mathbf{x})] = \sigma_{\text{CCD}}^2 \sum_{\Delta\mathbf{x}\in\mathcal{S}} s(\Delta\mathbf{x})^2, \qquad (12)$$

and the peak intensity in the filtered image is $\langle d_s(\mathbf{x}_k)\rangle = \alpha_k \sum_{\Delta\mathbf{x}\in\mathcal{S}} s(\Delta\mathbf{x})^2$; the SNR for the detection in the filtered image therefore writes

$$\text{SNR}_{d_s} = \frac{\langle d_s(\mathbf{x}_k)\rangle}{\sqrt{\text{var}[d_s(\mathbf{x}_k)]}} = \frac{\alpha_k}{\sigma_{\text{CCD}}}\sqrt{\sum_{\Delta\mathbf{x}\in\mathcal{S}} s(\Delta\mathbf{x})^2}. \quad (13)$$

The detection improvement by using the filtered image can be estimated from

$$\frac{\text{SNR}_{d_s}}{\text{SNR}_d} = \sqrt{\sum_{\Delta\mathbf{x}\in\mathcal{S}}\left(\frac{s(\Delta\mathbf{x})}{s(\mathbf{0})}\right)^2} \simeq 1.5, \qquad (14)$$

where the numerical value has been computed for our hardware and our settings. This means that by using the filtered image, the detection of local maxima is significantly more robust. This is of importance to detect the faintest events.

A threshold must be applied to validate a detection, otherwise local peaks due to the CCD noise could be confused with a real event. The threshold level can be derived according to probabilities. Assuming independent uniform Gaussian statistics for the noise and model errors, the probability that a pixel gets a value higher than ϵ is

$$\text{Pr}\{d(\mathbf{x}) \geq \epsilon\} = \frac{1}{2}\text{erfc}\left(\frac{\epsilon}{\sqrt{2}\sigma_{\text{CCD}}}\right). \qquad (15)$$

To have at most one false detection on an average per image, the threshold level must be such that $\text{Pr}\{d(\mathbf{x}) \geq \epsilon\} \leq 1/N_{\text{pix}}$, where N_{pix} is the number of pixels. For the 516×532 DALSA CA-D6 camera with $\sigma_{\text{CCD}} \simeq 0.5\,\text{DU}$, this yields $\epsilon \geq 4.4\sigma_{\text{CCD}} \simeq 2.2\,\text{DU}$. If the detection is performed in the filtered image, the minimum threshold value can be reduced, by a factor $\simeq 1.5$. Nevertheless, since (i) we have observed that the faintest events are mainly due to remanence, and (ii) we want to perform recentering (which requires sufficient discretization levels), we apply a higher threshold level ($\approx 5\,\text{DU}$ in practice). With such a high threshold, false events are negligible.

To summarize, our real-time detection method is performed as follows: the raw images are convolved by a 3×3 approximation of the shape of the events; in the filtered image, local maxima above a given threshold are selected and the 3×3 or 5×5 surrounding values are saved for further centering. Our detection method is reminiscent to the well-known technique of a matching filter, which as we have shown, yields the optimal local detection providing the shape of the events is known and the

noise can be approximated by uniform independent Gaussian statistics.

C. Fine Centering

It is well known that the simple photocenter computed from data restricted to a small area $\mathcal{S}$ is biased toward the geometrical center of $\mathcal{S}$. Various means to achieve better centering in the case of photon-counting data has been proposed by Michel *et al.* [23]. It is however possible to derive a centering method from our maximum likelihood approach. The criterion in Eq. (7) can be expanded as

$$\sigma_{\text{CCD}}^2\chi_{\text{local}}^2(\mathbf{x}_k, \alpha_k) = \sum_{\mathbf{x}\in\mathcal{S}_k} d(\mathbf{x})^2 - 2\alpha_k \sum_{\mathbf{x}\in\mathcal{S}_k} d(\mathbf{x})s(\mathbf{x}-\mathbf{x}_k)$$
$$+ \alpha_k^2 \sum_{\mathbf{x}\in\mathcal{S}_k} s(\mathbf{x}-\mathbf{x}_k)^2. \qquad (16)$$

By replacing α_k by its optimal value $\alpha_k^+(\mathbf{x}_k)$ given by Eq. (9), it comes that the optimal position is obtained by maximizing a criterion, which only depends on the position $\mathbf{x}_k$ of the event

$$\mathbf{x}_k^+ = \arg\max_{\mathbf{x}_k} \frac{\sum_{\mathbf{x}\in\mathcal{S}_k} d(\mathbf{x})s(\mathbf{x}-\mathbf{x}_k)}{\sqrt{\sum_{\mathbf{x}\in\mathcal{S}_k} s(\mathbf{x}-\mathbf{x}_k)^2}}. \qquad (17)$$

To achieve subpixel resolution, optimization of the criterion in Eq. (17) has to be done for fractional positions of the CCD pixel coordinates. Such an optimization can be done by a Newton method (e.g., the trust region Newton algorithm of Moré and Sorensen [24]) or by tabulating the values of $s(\mathbf{x}-\mathbf{x}_k)$ and $\sqrt{\sum_{\mathbf{x}\in\mathcal{S}_k} s(\mathbf{x}-\mathbf{x}_k)^2}$ for a predefined grid of subpixel positions. In any case, the event position $\mathbf{x}_k^+ = (x_k^+, y_k^+)$ given by Eq. (17) is slightly biased toward the center of the CCD pixel. Owing to the stability and the stationarity of the detector response, this bias can be easily fixed by means of histogram equalization of the subpixel positions [25].

As shown by Fig. 9, below, the proposed centering algorithm is effective, since it is able to recover the microchannel plate (MCP) structure (the microchannel pores are separated by $6\,\mu\text{m}$, which is $\sim 1/4$th CCD pixel after the optical demagnifier). However it relies on the assumed shape of the events and on the assumption that the CCD response is uniform across every individual pixel.

4. Spurious Events

We have seen that proper thresholding drastically reduces the probability of false detections due to the CCD noise. Among the detected events there can be other spurious events due to the amplifying stage defects. These spurious events can be caused by the dark current of the photocathode, by the remanence of the phosphor screens, and by positive ions at the input of the MCP.
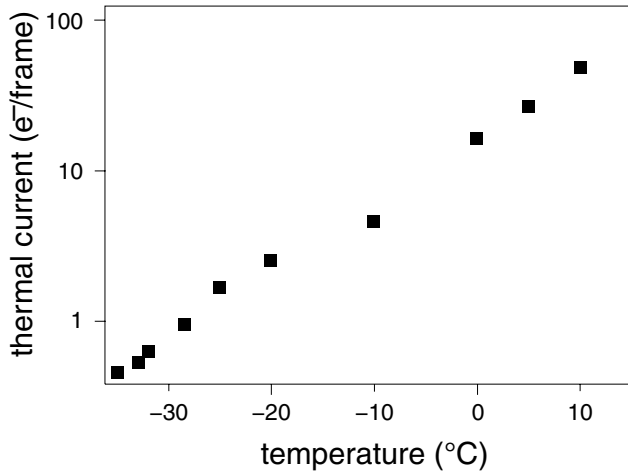
Fig. 4. Thermal current as a function of the temperature of the photocathode of the first light amplifier. Squares: measurements.

A. Dark Current

Unlike classical CCDs, the dark current of our camera is not due to the silicium of the CCD, but to the GaAs photocathode of the first intensifier. Indeed any thermal electron emitted by this photocathode is amplified as are the photon electrons. The gain of the first intensifier (10^4) is much larger than the amplitude of the photon-event dynamics, so the thermal electrons of the second intensifier do not sustain enough gain to be detected. We have measured the dark current over the temperature range between $16\,°C$ and $-35\,°C$, and checked that it fits the dark current law of a semiconductor.

The dark current n of the GaAs photocathode follows the Fermi–Dirac statistics:

$$n = N_c \exp\left(\frac{E_F - E_c}{k_B T}\right), \qquad (18)$$

where N_c is the equivalent state of density in the conduction band, E_F is the Fermi level of energy, E_c is the conduction level of energy, T is the temperature of the semiconductor, and k_B is the Boltzmann constant. The GaAs semiconductor can be considered as intrinsic, which means that it has as many electrons as holes, from what follows that

$$E_F - E_c = \frac{1}{2}\left[k_B T \log\left(\frac{N_v}{N_c}\right) - E_g(0\,°K)\right], \qquad (19)$$

where E_g is the gap of the semiconductor and N_v is the equivalent state of density in the valence band. Consequently the variations of our camera with temperature only depend on E_g and N_v.

We have fitted the thermal current measurements as a function of $1/T$ with a logarithmic regression for the lowest measured temperatures, where the gap is less sensitive to temperature variation (Fig. 4). We have derived $E_g \simeq 1.5\,eV$, which matches the physical value of the gap of an GaAs semiconductor ($E_G(0\,K) = 1.52\,eV$ for intrinsic GaAs [18]). Accord-

ing to our measurements and to the fitted law, we have chosen a working temperature of $-35\,°C$, for which we measure 0.45 counts per frame, which is equivalent to a very good thermal current of $5.5 \times 10^{-4}\,e^-/pixel/s$ or $\approx 2\,e^-/pixel/h$; the very best CCDs cooled to $-110\,°C$ or $-120\,°C$ reach the same dark current (in addition they also have a readout noise $\approx 2e^-/pixel$).

B. Remnant Events

The remanence of our camera is due to the temporal response of the phosphor screens, which causes the same event to be seen on more than one frame. This effect can be easily evidenced by measuring the spatiotemporal correlations of the detected events. Figure 5 shows correlation profiles as a function of the spatial distance $\Delta\mathbf{x}$ and for different temporal separations Δt. Since these profiles are computed from real data with a flat field, the profiles should be mostly flat functions if there is no remanence.

The excess counts for $|\Delta\mathbf{x}| \leq 1$ pixel in the cross correlation at $\Delta t = 1$ frame (dashed curve in Fig. 5) are due to remnant events, which are detected one more time in the next frame (possibly with a slight $|\Delta\mathbf{x}| = \pm 1$ pixel offset between consecutive frames due to the CCD noise, to the inhomogeneous microchannel recovery time, and to the influence of other close events). The profiles at different time offsets show that remanence is only significant for $\Delta t = 1$ frame and $|\Delta\mathbf{x}| \leq 1$ pixel. For this data set, there are about 25% of remnant events on an average; this is in agreement with the decay time of $\tau \sim 0.7\,ms$ given by the constructor data sheets for P43 phosphor screens of the light intensifiers.
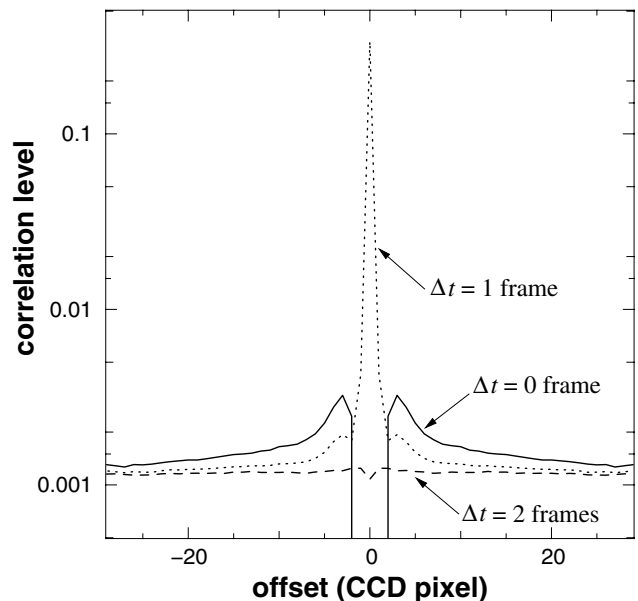

Fig. 5. Spatiotemporal correlation profiles. The curves show the average level of correlation of detected events as a function of the spatial separation and for different temporal separations Δt given in the number of 3.8 ms frames.

The depression $\Delta\mathbf{x} = \pm 1$ pixel in the autocorrelation ($\Delta t = 0$, solid curve in Fig. 5) is due to the inability to detect overlapping events; this is the so-called photon-counting hole [2,21,22]. Taking into account remanence, the photon-counting hole is a spatiotemporal volume of 3 pixels × 3 pixels × 2 frames, which matches our expectations from the physical spread and duration of the events and from the detection procedure.

In our data processing, the secondary events in pairs of events inside the photon-counting hole volume are considered as remnant ones and discarded. Note that removal of remnant events does not need to be done in real time, and we consider it as a postprocessing operation.

C. Ion Events

The last but not least kind of spurious events of our camera are ions in the multiplying stage. Ion events are created by the detachment of positive ions at the input of MCPs. When we built our cameras, intensifiers with a semiconductor photocathode were equipped with a special film, which performs as an ion barrier to protect the photocathode. Some ions may however cross the barrier and get accelerated back to the photocathode. Photocathodes are coated with aluminum to lengthen their lifetime regarding such ion impacts. The newest intensifiers no longer need such films, which slightly reduce the quantum efficiency.

Each ion impact creates a burst of electrons, whose amplification in the multiplying stage results in a giant ion event on the CCD (Fig. 6). Thanks to their large spatial extension, ion events can be rejected in real time. We have indeed checked that the ratio between the peak intensity of a detected event and the intensities of its four neighbor pixels provides us with a reliable criterion to reject all the ions.

5. Performances of the Camera

A. Photon-Counting Hole and Saturation

The photon-counting hole sets a limitation for the maximum number of photons that can be detected in a single CCD frame. Assuming a uniform incident flux with N incident events on the CCD per frame, it can be shown [22] that the actual number $\tilde{N}$ of detected photons accounting for the loss due to the overlapping of the events reads

$$\tilde{N} \simeq N \exp(-\beta N), \qquad (20)$$

where β is the ratio between the photon-counting hole area and the CCD area. On the basis of a maximum of 20% loss of linearity of the counting mode and with a 3 × 3 pixel hole (hence $\beta \simeq 3.3 \times 10^{-5}$ for a CPNG camera), we find that $N \leq 7 \times 10^3$ events/frame, which corresponds to a "saturation" flux of ~ 7 events/pixel/s.

To reduce the effects of overlapping and to limit the size of the photon-counting hole, we have modified
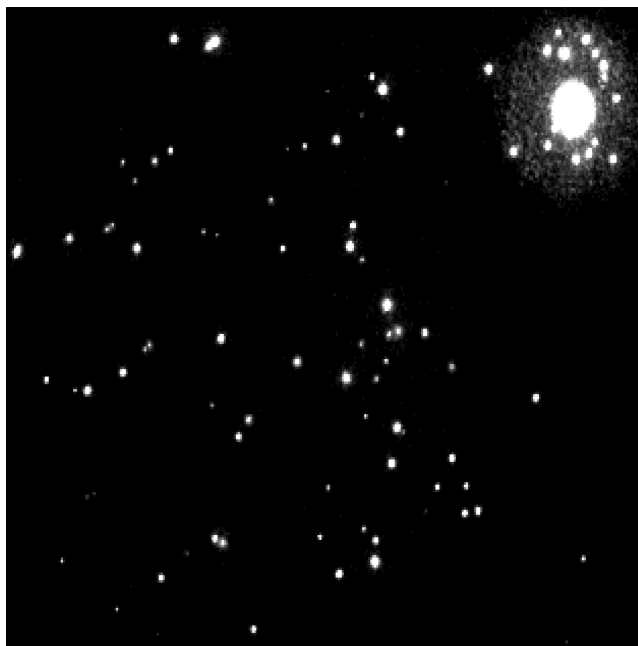

Fig. 6. Single ICCD image showing a large event burst in the top right corner due to an ion.

our maximum likelihood detection of a single event, by taking into account a nonzero background (namely a constant plus a slope) in the model assumed for the detection. Since s (see Subsection 3.A) is an even function, this is simply achieved by filtering the raw image by

$$s^\star(\Delta\mathbf{x}) = s(\Delta\mathbf{x}) - \langle s(\Delta\mathbf{x}) \rangle_{\Delta\mathbf{x}\in\mathcal{S}} \qquad (21)$$

instead of s. As shown by the mean autocorrelation in Fig. 7, this simple modification has effectively reduced the photon-counting hole to its smallest size (3 × 3 pixels) even at relatively high fluxes.

B. Quantum Efficiency

To measure the quantum efficiency, we have build low-flux sources at different wavelengths, using temperature stabilized light emitting diodes. Their fluxes have been measured with a calibrated photodiode. We have used a calibrated neutral density filter to reduce the flux so as not to saturate. The global flux precision is about 2%. Ideally the quantum efficiency should be that of the first photocathode, but some losses are expected.

We have measured the number of real events detected with the different calibration sources by our CPNG cameras (with the GaAsP light intensifier and the GaAs one) as follows. First we have rejected the ion events and also the events due to remanence by means of spatiotemporal cross correlations. From the remaining number of detected events, we subtracted the mean counts due to the thermal current. Figure 8 shows the QE measured for our CPNG cameras. It reaches up to 26% for the GaAs photocathode, and 36% for the GaAsP one. This effective QE is a dramatic improvement compared to the QE $\sim 4\%$
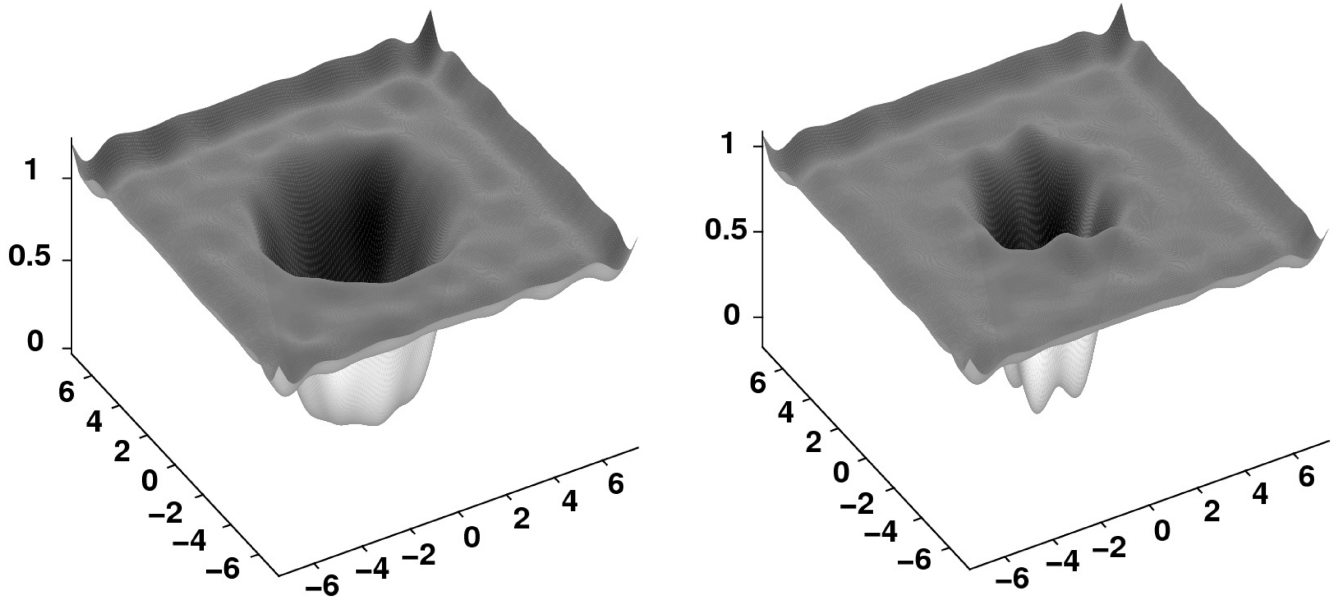
Fig. 7. Two-dimensional mean spatial autocorrelations of photon events. Left: raw correlation. Right: some possible overlapping of the photon events is taken into account, which reduces the photon-counting hole to its limit of 3 × 3. Hence the saturation flux (the possible detection area for a single event) is improved.

for the previous generation of photon-counting cameras (CP40).

Such an increase of sensitivity is due to the improved intrinsic sensitivity of the photocathodes, to the reduction of the microchannels obstruction factor, but also to our careful processing of the raw image data thanks to which very few events are lost by the detection algorithm. The fits in Fig. 8 also show that losses between the photocathode sensitivity and our measured sensitivity are achromatic. The effective QE of the photon-counting camera can therefore be expressed as

$$\eta(\lambda) = \eta_{ph}(\lambda)\eta_{loss}, \qquad (22)$$

where η_{ph} is the photocathode sensitivity and η_{loss} is the efficiency of the amplification and detection stages. Taking into account the various independent defects responsible for the sensitivity loss, η_{loss} can be factorized as

$$\eta_{loss} = \eta_{mc}\eta_{ion}\eta_{sat}, \qquad (23)$$

where η_{mc}, η_{ion}, and η_{sat} are the attenuation factors, respectively, due to the MCP obstruction, to the anti-ion film, and to the saturation of the counting mode. Since our calibrations have been done under very low photon fluxes, we have $\eta_{sat} \simeq 1$. Using our measurements, our model of the saturation loss and the data sheets of the photocathodes, we find that $\eta_{mc} \times \eta_{ion} \simeq 0.65$, which agrees with the MCPs data sheets.

C. Spatial Resolution

To test the ability of our maximum likelihood algorithm to properly estimate event positions with subpixel accuracy, we averaged the autocorrelations of photon-counting images under uniform illumination (flat field) and with a superresolution of 1/20th pixel. The honeycomb structure of the microchannel pores can be clearly seen in Fig. 9, which shows the central part of the average autocorrelation. Taking into
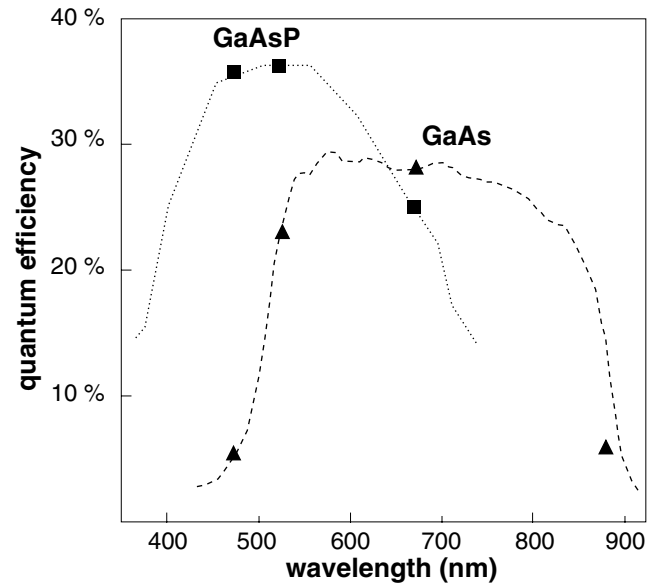

Fig. 8. QE of CPNG/Algol cameras as functions of the wavelength. The squares and triangles indicate our measurements and the curves are the spectral responses of the photocathodes provided by the constructors data sheets and scaled to fit our data. The precision comes from the sources fluxes: 2%.
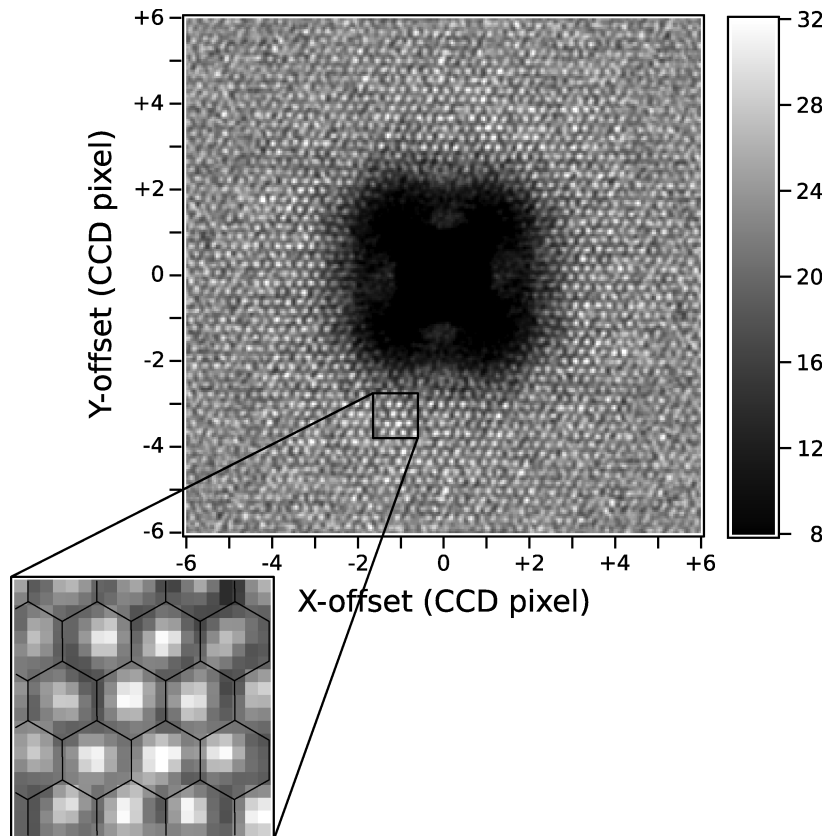
Fig. 9. Mean autocorrelation of detected event positions under flat field and computed with a resolution of 1/20th of a CCD pixel. Axes are labeled in pixel units. The accurate event positions were determined by a maximum likelihood fit followed by histogram equalization of the subpixel positions to avoid the bias of the centering method. The honeycomb structure of the microchannel arrays (seven fibers per pack) is clearly seen in the one squared CCD pixel zoomed area. The dark part around the coordinates $(0, 0)$ is due to the photon-counting hole.

account the optical magnification, the ∼1/4th CDD pixel size of the honeycomb structure in Fig. 9 matches the separation of 6 μm of the microchannel pores. In practice, there is no means to determine the position of incident events with a better resolution than that of the microchannels, which is much coarser than the accuracy achievable by the fine centering of events. The effective spatial resolution of our photon-counting cameras is therefore limited by the microchannels structure to ∼1/4th CDD pixel. In the photon-counting mode, CPNG and Algol are equivalent to 2D cameras with ∼2000 × 2000 to ∼3000 × 3000 effective pixels depending on the optical setup.

6. Conclusions

Today, six Algol-CPNG ICCDs have been built. New microchannels and image processing enable us to reach up to 36% and 26% QE in the blue (GaAsP) and in the red (GaAs), respectively; this is 65% of the QE of these photocathodes. It is a marked increase in the sensitivity compared to the previous (CP40) ones. Thanks to the new photon centroiding algorithm, which we have developed, there are no traces of the CCD pixels in the super resolution images (1 logical pixel = 1/(4 × 4) CCD pixel), so that the resolution is only limited by the size of the individual microchannels.

These new ICCDs are the most suitable ones for high angular resolution observations in the visible at 8 – 10 m class telescope and at large interferometers. The increase of limiting magnitudes of our instruments will open new classes of objects to observations at high angular resolution. From mid 2003 to 2005, both Algol cameras were used on the GI2T-REGAIN interferometer. Now the spectrograph of REGAIN and the Algol cameras are installed at the Center for High Angular Resolution Astronomy (CHARA) interferometer. SPID is being modified to match the photocathode diameter smaller than the CP40 one.

For biological applications, the high QE of the camera will enable us to get images at the optimum resolution given the selected objective, and a frame by frame photon count will provide us with a unique possibility to simultaneously monitor the time event of photon emission, possibly opening a field of investigations on the kinetics of photobiochemical reactions.

References

1. A. Blazit, "A 40-mm photon counting camera," Proc. SPIE **702**, 259–263 (1987).

2. R. Foy, "The photon counting camera CP40," in *Instrumentation for Ground-Based Optical Astronomy, Present and Future*, Lick Observatory, eds. (Springer-Verlag, 1988), pp. 589.

3. D. Mourard, L. Abe, A. Domiciano de Souza, D. Bonneau, A. Blazit, F. Vakili, and P. Stee, "Status report on the GI2T interferometer," Proc. SPIE **4838**, 9 (2003).

4. M. Tallon, A. Baranne, A. Blazit, F.-C. Foy, R. Foy, I. Tallon-Bosc, and E. Thiébaut, "SPID, a high spectral resolution diffraction limited camera," Proc. SPIE **4007**, 962 (2000).

5. D. Mourard, D. Bonneau, J. M. Clausse, F. Hénault, A. Marcotto, A. Blazit, S. Bosio, Y. Bresson, T. ten Brummelaar, P. Kervella, S. Lagarde, H. A. McAlister, A. Mérand, G. Merlin, N. Nardetto, R. Petrov, A. Roussel, K. Rousselet-Perraut, P. Stee, J. Sturmann, L. Sturmann, and I. Tallon-Bosc, "VEGA: a visible spectrograph and polarimeter for CHARA," Proc. SPIE **6268**, 626803-1–11(2006).

6. P. Stee, D. Mourard, D. Bonneau, P. Berlioz-Arthaud, A. Domiciano de Souza, R. Foy, P. Harmanec, S. Jankov, P. Kervella, P. Koubsky, S. Lagarde, J.-B. Le Bouquin, P. Mathias, A. Mérand, N. Nardetto, R. G. Petrov, K. Rousselet-Perraut, C. Stehle, and G. Weigelt, "VEGA: a visible spectrograph and polarimeter for CHARA—science cases description," Proc. SPIE **6268**, 62683R-1–22 (2006).

7. R. Foy, D. Bonneau, and A. Blazit, "The multiple QSO PG1115 + 08—A fifth component?," Astron. Astrophys. **149**, L13–L16 (1985).

8. R. S. Negrin and C. H. Contag, "In vivo imaging using bioluminescence: a tool for probing graft-versus-host disease," Nat. Rev. Immun. **6**, 484–490 (2006).

9. A. Roda, P. Pasini, M. Mirasoli, E. Michelini, and M. Guardigli, "Biotechnological applications of bioluminescence and chemiluminescence," Trends Biotechnol. **22**, 295–303 (2004).

10. L. F. Greer, III and A. A. Szalay, "Imaging of light emission from the expression of luciferases in living cells and organisms: a review," J. Lumin. **17**, 43–74 (2002).

11. R. T. Sadikot and T. S. Blackwell, "Bioluminescence imaging," Proc. Am. Thorac. Soc. **2**, 537–540 (2005).

12. P. Maechler, H. Wang, and C. B. Wollheim, "Continuous monitoring of ATP levels in living insulin secreting cells expressing cytosolic firefly luciferase," FEBS Lett. **422**, 328–332 (1998).

13. H. J. Kennedy, A. E. Pouli, E. K. Ainscow, L. S. Jouaville, R. Rizzuto, and G. A. Rutter, "Glucose generates sub-plasma membrane ATP microdomains in single islet beta-cells. Potential role for strategically located mitochondria," J. Biol. Chem. **274**, 13281–13291 (1999).

14. J.-L. Gach, O. Hernandez, J. Boulesteix, P. Amram, O. Boissin, C. Carignan, O. Garrido, M. Marcelin, G. Östlin, H. Plana, and R. Rampazzo, "Fabry–Pérot observations using a new GaAs photon-counting system," in *Scientific Detectors for Astronomy, The Beginning of a New Era*, P. Amico, J. W. Beletic, and J. E. Beletic, eds. (Kluwer Academic, 2002), pp. 335–339.

15. P. Jerram, P. Pool, R. Bell, D. Burt, S. Bowring, S. Spencer, M. Hazelwood, I. Moody, N. Catlett, and P. Heyes, "The LLLCCD: low light imaging without the need for an intensifier," in *Sensors and Camera Systems for Scientific, Industrial, and Digital Photography Applications II*, (SPIE, 2001), pp. 178–186.

16. M. S. Robbins and B. J. Hadwen, "The noise performance of electron multiplying charge-coupled devices," IEEE Trans. Electron Devices **50**, 1227–1232 (2003).

17. A. G. Basden, C. A. Haniff, and C. D. MacKay, "Photon counting strategies with low-light level CCDs," Mon. Not. R. Astron. Soc. **345**, 985–991 (2003).

18. O. Madelung, M. Schulz, and H. Weiss, "Intrinsic properties of group IV elements and III-V, II-VI, and I-VII compounds," in *Landolt-Bornstei, New Series, Group III* (Springer, 1987).

19. C. G. Coates, D. J. Denvir, N. G. McHale, K. D. Thornbury, and M. A. Hollywood, "Optimizing low-light microscopy with back-illuminated electron multiplying charge-coupled device: enhanced sensitivity, speed, and resolution," J. Biomed. Opt. **9**, 1244–1252 (2004).

20. J.-L. Gach, C. Guillaume, O. Boissin, and C. Cavadore, "First results of an L3CCD in photon counting mode," in *Astrophysics and Space Science Library* (2004), pp. 611–614.

21. E. Thiébaut, "Speckle interferometry with a photon-counting detector," Astron. Astrophys. **284**, 340–348 (1994).

22. E. Thiébaut, "Avoiding the photon-counting hole in speckle imaging by means of cross-correlation techniques," J. Opt. Soc. Am. A **14**, 122–130 (1997).

23. R. Michel, J. Fordham, and H. Kawakami, "Fixed pattern noise in high-resolution, CCD readout photon-counting detectors," Mon. Not. R. Astron. Soc. **292**, 611–620 (1997).

24. J. J. Moré and D. C. Sorensen, "Computing a trust region step," SIAM (Soc. Ind. Appl. Math.) J. Sci. Stat. Comput. **4**, 553–572 (1983).

25. M. K. Carter, R. Cutler, B. E. Patchett, P. D. Read, N. R. Waltham, and I. G. van Breda, "Transputer-based image photon-counting detector," in Instrumentation in Astronomy VII, Proc. SPIE **1235**, 644–656 (1990).